




Article

# Evaluating the Impact of Filtering Techniques on Deep Learning-Based Brain Tumour Segmentation

Sofia Rosa <sup>1,†</sup> , Verónica Vasconcelos <sup>1,2,†</sup>  and Pedro J. S. B. Caridade <sup>3,\*,†</sup> 

<sup>1</sup> Coimbra Institute of Engineering, Polytechnic University of Coimbra, Rua da Misericórdia, Lagar dos Cortiços, S. Martinho do Bispo, 3045-093 Coimbra, Portugal; sofiasousa1311@gmail.com (S.R.); veronica@isec.pt (V.V.)

<sup>2</sup> INESC TEC—Institute for Systems and Computer Engineering, Technology and Science, Campus da Faculdade de Engenharia da Universidade do Porto, Rua Dr. Roberto Frias, 4200-465 Porto, Portugal

<sup>3</sup> Coimbra Chemistry Center—Institute of Molecular Sciences (CQC-IMS), Department of Chemistry, University of Coimbra, 3004-535 Coimbra, Portugal

\* Correspondence: pedrojcaridade@uc.pt

† These authors contributed equally to this work.

**Abstract:** Gliomas are a common and aggressive kind of brain tumour that is difficult to diagnose due to their infiltrative development, variable clinical presentation, and complex behaviour, making them an important focus in neuro-oncology. Segmentation of brain tumour images is critical for improving diagnosis, prognosis, and treatment options. Manually segmenting brain tumours is time-consuming and challenging. Automatic segmentation algorithms can significantly improve the accuracy and efficiency of tumour identification, thus improving treatment planning and outcomes. Deep learning-based segmentation tumours have shown significant advances in the last few years. This study evaluates the impact of four denoising filters, namely median, Gaussian, anisotropic diffusion, and bilateral, on tumour detection and segmentation. The U-Net architecture is applied for the segmentation of 3064 contrast-enhanced magnetic resonance images from 233 patients diagnosed with meningiomas, gliomas, and pituitary tumours. The results of this work demonstrate that bilateral filtering yields superior outcomes, proving to be a robust and computationally efficient approach in brain tumour segmentation. This method reduces the processing time by 12 epochs, which in turn contributes to lowering greenhouse gas emissions by optimizing computational resources and minimizing energy consumption.

**Keywords:** brain tumours; segmentation; CE-MRI; convolutional neural networks; U-Net; filtering



**Citation:** Rosa, S.; Vasconcelos, V.; Caridade, P.J.S.B. Evaluating the Impact of Filtering Techniques on Deep Learning-Based Brain Tumour Segmentation. *Computers* **2024**, *13*, 237. <https://doi.org/10.3390/computers13090237>

Academic Editors: Mads Sloth Vinding, Ivan Maximov, Christoph Stefan Aigner and Paolo Bellavista

Received: 8 July 2024

Revised: 28 August 2024

Accepted: 13 September 2024

Published: 18 September 2024



**Copyright:** © 2024 by the authors. Licensee MDPI, Basel, Switzerland. This article is an open access article distributed under the terms and conditions of the Creative Commons Attribution (CC BY) license (<https://creativecommons.org/licenses/by/4.0/>).

## 1. Introduction

In recent years, there has been a considerable increase in medical cases involving brain tumours, making them the tenth most prevalent type of tumour affecting both adults and children [1]. A brain tumour is the growth of abnormal cells in brain tissues and is classified as primary or secondary. The most prevalent types of brain tumours are gliomas and meningiomas, making them significant areas of focus in neuro-oncology. Gliomas are tumours that arise from glial cells that support and protect neurones in the brain and spinal cord. Meningiomas, on the other hand, originate in the meninges, the protective membranes of the brain and spinal cord. Secondary tumours arise from existing ones in other parts of the body and later spread to different organs and systems through metastasis. In contrast, primary tumours are caused by nerve tissue or meninges cells [2]. Gliomas are classified by the World Health Organisation (WHO) in grades I to IV, depending on their microscopic appearance [3].

Many procedures, such as magnetic resonance imaging (MRI) and computer tomography (CT), help physicians diagnose brain tumours. Following the identification of tumours, a biopsy may be indicated. Although a biopsy will reveal whether there is a tumour or not,

its location must be known before surgery [4]. Targeted treatments and immunotherapies can improve treatment efficacy and even cure specific brain tumour subtypes [5]. Advancements in MRI have significantly improved patient outcomes by early detection of brain tumours, becoming the most popular technique for non-intrusive detection [6]. MRI is used to recognise flowing blood, visualise detailed brain characteristics (and other cranial structures), and visualise the brain's anatomy in three different planes: axial, coronal, and sagittal. MRI is also very effective in the detection of other brain-related diseases, such as Alzheimer's disease, Parkinson's disorder, or dementia [1]. Compared to CT, MRI has the advantage of not using ionising radiation and provides greater contrast between soft tissues [7].

Sophisticated algorithms and methods are being developed to identify the form, shape, and stage of brain tumours in the imaging field (see, e.g., ref. [8]). Some diagnostics continue to rely on manual segmentation [9], which has several major limitations. It is quite time-consuming and requires significant work from radiologists. Subjective analysis generates inconsistencies because different professionals might segment the same image in various ways [10]. Repetitive tasks can cause fatigue, increase the risk of errors, and reduce accuracy over time. Statistics indicate that radiologists miss 10% to 30% of tumours during routine screening [4]. Furthermore, manual segmentation is not easily scalable to large volumes of data, making it impractical for large-scale studies [11]. Updating or reanalysing old data is very difficult, and the methodology may miss minor or subtle traits that automated methods would find.

Computer-aided systems are being used to improve medical diagnostics and treatment recommendations. Some methods used in image segmentation are threshold, region-based, supervised, and unsupervised classification techniques [4,12]. A large number of frameworks and methods have been proposed for automatic detection and segmentation. Algorithms based on hybrid fuzzy  $k$ -mean [13], maximum likelihood estimation-assisted kernel principal component analysis [14], and Gaussian hybrid fuzzy clustering [15] have been proposed for the task of segmentation. Many machine learning algorithms have also been extensively used to categorise brain tumours. In recent years, deep learning has shown enormous potential in the field of image segmentation [16–18] and in the segmentation of brain tumours [19–22], employing various neural network architectures to increase accuracy and efficiency. Convolutional neural networks (CNNs) have proven particularly effective, with models such as U-Net and its variants in widespread use. For example, on the BraTS 2020 challenge dataset [23], a deep learning-based solution, the U-Net architecture with edge-enhancing diffusion filtering and attention modules allowed high values of sensitivity. Deep CNNs trained on the BraTS dataset [23] have achieved a validation accuracy of 98%, highlighting the robustness of these models in the identification and segmentation of brain tumours [24]. Other studies have explored various deep learning models, including recurrent residual U-Net, which has demonstrated its effectiveness in brain tumour segmentation [20]. Techniques such as fuzzy C-means and optimisation algorithms have also been used to improve segmentation accuracy [25]. The dual convolution tumour network model integrates dual CNNs with the VGG16 architecture to improve recognition and classification tasks beyond conventional approaches [26]. In [27], the binomial threshold-based bidirectional long-short-term memory (BT-Bi-LSTM) model is proposed. MRI from the 2019 and 2020 BRATS datasets is pre-processed using normalisation and contrast-limited adaptive histogram equalisation (CLAHE). Segmentation is carried out using the binomial threshold technique, and features are extracted using the grey-level co-occurrence matrix and local binary pattern. In general, deep learning has significantly improved the accuracy and efficiency of brain tumour segmentation, helping to refine diagnosis and treatment planning using deep learning methodologies [26].

Combined frameworks, like the ensemble approach of 3D CNN and U-Net models, have shown promising results. Comparative studies between U-Net, residual network, and multi-ResNet architectures demonstrate that multi-ResNet achieved superior performance in accurately separating tumour regions and capturing high-level features of brain images

in benchmark datasets [28,29]. Multimodal deep learning models based on U-Net and VGG16 architectures have been effective in segmenting subregions that achieve high metric values [30]. The combination of the U-Net and 3D-CNN [28] models has been used to achieve precise predictions. An automated segmentation method has been devised for the separation of tumours from MRI scans [31]. In addition, a classification system has been created based on weighted characteristics and ensemble learning [32].

With the success of U-Net, several improvements have been proposed. Zhou et al. [33] developed U-Net++, an innovative segmentation architecture that utilises nested and dense skip connections. The core idea is that the model can capture fine-grained details of foreground objects more effectively by gradually enriching the high-resolution feature maps of the encoder before fusing them with semantically rich feature maps from the decoder [33]. Micallef et al. [34] used a variation of U-Net++ by changing the number of convolution blocks, the skip connection system, and using a loss function different from the original U-Net++. The authors reduced the number of parameters by half in relation to the original U-Net++. Huang et al. [35] introduced U-Net3+, a network that uses full-scale skip connections to integrate high- and low-level semantics at various scales, improving segmentation accuracy. Each encoder in U-Net3+ consists of two convolutional layers with a  $3 \times 3$  kernel, which contributes significantly to improved performance. The encoder extracts abstract features from the input image, with varying degrees of abstraction on scales. Higher abstraction is crucial for subsequent network stages. During upsampling, the integration of semantic information from the encoder via skip connections significantly boosts segmentation accuracy. Qi et al. [36] replaced the batch normalisation layer with the filter response normalisation layer to eliminate the impact of batch size on U-Net3+, also employing the encoder based on the residual structure of the stage.

Concurrently, with the ongoing development of segmentation algorithms, a crucial factor is the quality of the images used to train the network. Despite many MRI apparatuses being state-of-the-art, the data acquired are affected by noise, which increases the complexity of the diagnosis process. Noise is introduced due to an erroneous imaging environment or processing in noisy transmission systems [37]. Noise manifests as blurred areas, unpredictable fluctuations, pixelization of borders, and distortions. Moreover, indistinguishable anatomical boundaries containing substantial information and low spatial resolution negatively impact the effectiveness of computer analysis [38]. Several denoising techniques have been proposed in recent years (see refs. [39–43] and the references therein).

In this work, the impact of four denoising filters in tumour detection and segmentation is examined by performing a systematic scan of the most relevant parameters present in the median, Gaussian, anisotropic diffusion, and bilateral filters. For segmentation, the U-Net framework has been employed in contrast-enhanced magnetic resonance imaging (CE-MRI). A recent review studied the environmental sustainability and the use of artificial intelligence in radiology [44]. Medical imaging accounts for 1% of global greenhouse gas (GHG) emissions in the USA, mainly due to the manufacture of the apparatus. However, the increasing use of machine learning algorithms in diagnostic-assisted methodologies is leading to a substantial increase in emissions. To reduce such an environmental footprint, one may adopt energy-efficient computational hardware and balance the computational cost/computational time required with the accuracy achieved, in this case, without sacrificing the diagnostic quality. Due to the high impact of artificial intelligence methods on environmental sustainability, particularly in radiation [44], performance comparison covers not only the statistical metrics of segmentation quality but also the computational time and computational cost [45–48].

## 2. Algorithm, Dataset, and U-Net Architecture

The dataset [49] used in this work contains 3064 contrast-enhanced magnetic resonance images (CE-MRI) weighed on T1 from 233 patients with three types of brain tumours: meningioma (708 slices), glioma (1426 slices), pituitary tumour (930 slices), and their respective segmentation masks, delineated by three experienced radiologists. The brain T1-

weighted CE-MRI dataset was acquired from Nanfang Hospital, Guangzhou, China, and General Hospital, Tianjing Medical University, China, from 2005 to 2010. The images have an in-plane resolution of  $512 \times 512$  with pixel size  $0.49 \times 0.49 \text{ mm}^2$ , while the slice thickness is 6 mm and the slice gap is 1 mm. From the dataset and their respective masks [49], 60% that were randomly chosen have been selected for training (1840 images), 20% for validation (612 images), and 20% for testing (612 images).

The current analysis of the impact of denoising MRI employed the U-Net [50] architecture, as it is a low-parameter architecture that provides good results when using small datasets. Larger datasets can be found in the literature [23], but the computational cost would increase substantially and is outside the scope of this work. As stated in the Introduction, many U-Net variations have been proposed but are associated with higher computational costs and larger datasets. The U-Net architecture [50] comprises two branches arranged in a U-shaped form: an encoder branch (contracting path) and a decoder branch (expanding path). In Algorithm 1, the structure employed in this work is briefly described, while Table 1 gathers the hyperparameters used in the network. The U-Net [50] algorithm has been implemented in Python using the TensorFlow library [51].

**Table 1.** Hyperparameter values for the U-Net model employed in this work.

Parameters	Values
Learning rate	$1 \times 10^{-4}$ – $1 \times 10^{-7}$
Batch size	115
Epochs	300
Optimiser	Adam
Filter size	$3 \times 3, 2 \times 2$
Activation function	ReLU, sigmoid

The encoder branch structure mirrors CNNs with convolutional operations followed by downsampling for feature extraction [52]. In the decoder branch, an upsampling and concatenation layer is followed by regular convolutional operations [50,53]. This process allows the decoder branch to apply learnt discriminate features to the pixel space through the encoder network, enabling dense classification [54]. A skip connection between equivalent layers of the encoder and decoder facilitates concatenating feature maps from the encoder network with the up-sampled feature map, providing coarse global contextual information. This method helps to recover local characteristics during the downsampling technique [55].

The U-Net model used contains the contracting path features with eight convolutional layers. The purpose of the convolution layer is to calculate the weights of the kernels that perform the convolution operation on the images (see, e.g., ref. [56] and the references therein). The operation has two tensors as input and produces one tensor as output. Typically, one tensor represents an image, and the other represents a kernel (filter). Each element of one tensor is multiplied by the correspondent element of the second tensor, and then all values are summed [57]. The general convolution operation between an image and a kernel is given as follows:

$$I_c(x, y) = (\mathbf{I} \times \mathbf{K})_{xy} = \sum_{s=-a}^a \sum_{t=-b}^b K(s, t) I(x-s, y-t), \quad (1)$$

where  $m$  and  $n$  are the size of the kernel and  $a$  and  $b$  are obtained through  $a = (m-1)/2$  and  $b = (n-1)/2$ . The chosen kernel has a size of  $3 \times 3$ . When dealing with images, it is not optimal for the result of a convolution operation to have dimensions different from the original image. Padding is used to address this by adding rows of pixels to the top and bottom and columns to the right and left of the image, ensuring that the resulting matrices retain the same size as the original [58].

After each convolution operation, a batch normalisation layer is applied to make the whole model more efficient, normalising the activation to have a zero mean and unit

variance [59]. Subsequently, the rectified linear unit (ReLU) activation function is applied. Since convolution is a linear operation and the images are far from linear, non-linearity layers are often placed directly after the convolutional layer to introduce non-linearity to the activation map [60]. The non-linear operations used in this work have been ReLU,  $f(k) = \max(0, k)$  [61], and sigmoid-type  $\sigma(k) = [1 + \exp(-k)]^{-1}$  [60].

---

**Algorithm 1:** Brain tumour Segmentation with U-Net
 

---

**Input:** MRI Brain tumour; MRI Brain tumour dataset

**Data:** learning rate = 0.0001; optimiser = adam; loss = dice loss; epochs = 300; steps per epoch = 30

**while** # images in dataset **do**  
 | read image & mask; resize and normalise mask  
**end**

**for** each filter **do**  
 | apply filter; resize and normalise image  
**end**

**set machine-learning:** divide dataset: 60% train + 20% validation + 20% test;  
 define U-Net model

$i = 0; k = 0$   
**while**  $i \leq 9$  **do**  
 | conv2d( $i$ )  
 | batch( $i$ )  
 | activation( $i$ )  
 | **if**  $\text{mod}(i + 1, 2) = 0 \ \& \ i \leq 7$  **then**  
 | | maxpooling( $k$ )  
 | |  $k++$   
 | **end**  
 |  $i++$

**end**  
 $k = 0$   
**while**  $k \leq 3$  **do**  
 | conv2dtranspose( $k$ )  
 | concatenate( $k$ )  
 |  $j = 0$   
 | **while**  $j \leq 1$  **do**  
 | | conv2d( $i$ )  
 | | batch( $i$ )  
 | | activation( $i$ )  
 | |  $j++; i++$   
 | **end**  
 |  $k++$

**end**

U-Net(model=train)

U-Net(model=test)

**if** detected tumour **then**  
 | **output:** mask  
**end**

---

The contracting path is defined by the encoder block function that performs convolution and batch normalisation operations, followed by a  $2D$  maximum pooling layer with a  $2 \times 2$  kernel size. The pooling layer involves the down-sampling operation that leads to a reduction in the dimensionality of the training data and also drastically reduces the number of parameters in the input [62]. The expanding path employs a transposed convolution layer to perform upsampling of the data while the skipped features are concatenated. This concatenation allows for recovering spatial details lost during downsampling in the contracting path. After concatenation, convolution, batch normalisation, and ReLU activation operations are applied again. Finally, the output layer is a  $2D$  convolutional layer with a single output and sigmoid activation, which generates the segmentation mask of the brain tumour.

Image pre-processing is the initial step in enhancing image quality. It includes artefact removal, skull despoliation, noise reduction, and overall image improvement. These processes are essential for the rapid detection of malignancies [39]. MRI denoising is a critical medical imaging procedure that aims to enhance the quality of images by reducing noise and artefacts that can obscure essential details necessary to perform a correct diagnostic. Magnetic resonance imaging is frequently marred by speckle noise [63], salt & pepper noise [64], and Gaussian noise [65] when acquired and transmitted. In general, noise in the MR image is characterised by Rician distribution. Many algorithms have been suggested to eliminate these types of noise (see refs. [9,14,39,66] and the references therein). As stated earlier, one of the goals of this work is to systematically study the impact of smooth-filtering in original images for the detection and segmentation of tumours.

Four filters have been used in this work: (i) median [14], (ii) Gaussian [15], (iii) anisotropic diffusion [67], and (iv) bilateral [68].

The median filter is a non-linear, statistical filter. Unlike linear filters such as mean and Gaussian filters, which can smooth and blur the image, the median filter preserves significant information by avoiding extreme values. However, it can still smooth out fine details. The noisy value in an image  $f(I_{\mathcal{N}})$  is replaced by the median value of the pixels in the surrounding neighbourhood [14]:

$$I_m(x, y) = \text{median}(I_{\mathcal{N}}(x, y)). \quad (2)$$

The key parameter in the median filter is the kernel size  $\mathcal{N} \otimes \mathcal{N}$ . Several studies have shown that a large kernel size leads to extensive smoothing out, leading to the disappearance of the details of images. The lower values of the kernel,  $\mathcal{N} = 3$ , are optimal to maintain the most relevant characteristics for segmentation. For the median filter, no further analysis has been carried out.

The Gaussian filter,  $g(s, t)$ , is a linear isotropic low-pass filter that attenuates the high frequencies associated with noise. The filter is usually defined as Gaussian:

$$g(s, t) = \frac{1}{2\pi\sigma} \exp\left(-\frac{s^2 + t^2}{2\sigma^2}\right), \quad (3)$$

converting the original image into [15]

$$I_g(x, y) = \sum_{s=-a}^a \sum_{t=-a}^a g(s, t) I(x - s, y - t). \quad (4)$$

Gaussian filter is also applied in the pre-processing phase before applying differential operators, which emphasise noise, and before building multi-resolution structures, helping to minimise aliasing artefacts and producing better quality resized images. The parameter  $\sigma$  of the Gaussian filter determines the level of smoothing, requiring a value that balances noise reduction and preservation of detail. In this particular case, the width of the Gaussian was calculated using the following kernel size:



$$\sigma(K) = \frac{3}{10} \left[ \frac{1}{2}(K-1) - 1 \right] + \frac{4}{5}. \quad (5)$$

Common kernel values are available in the literature for  $3 \times 3$  and  $5 \times 5$  [15] and for larger images,  $7 \times 7$  [69] is used for extensive noise reduction. These values are used to analyse the impact in the segmentation.

In magnetic resonance magnitude images, noise leads to image intensity being governed by a Rician distribution, resulting in bias at low signal intensities [70]. Therefore, traditional noise reduction technologies, such as Gaussian filters and median filters, are not very effective in these cases. Anisotropic diffusion is a non-linear iterative filtering technique that promotes diffusion in the homogeneous region while inhibiting diffusion at the edges. The partial differential equation of anisotropic diffusion to be solved is as follows [67]:

$$\frac{\partial I(x, y, t)}{\partial t} = \text{div}[C(x, y, t) \nabla I(x, y, t)], \quad (6)$$

where  $\text{div}$  is the divergent operator,  $\nabla$  is the gradient, and  $C$  is the diffusion coefficient that controls the diffusion strength, while  $t$  is the process-ordering parameter used in the discrete implementation to enumerate the iteration steps. The initial condition to feed the equations is the image before applying the filter  $I_0 \equiv I(x, y, t = 0)$ . The diffusion function  $C$  depends on the magnitude of the gradient of the image intensity, and is a monotonically decreasing function. It mainly diffuses within regions and does not affect region boundaries at locations of high gradients. Two different diffusion functions have been used [67]:

$$C_1(x, y, t) = \exp\left[-(|\nabla I(x, y, t)| \times \mathcal{K}^{-1})^2\right], \quad (7)$$

$$C_2(x, y, z) = [1 + (|\nabla I(x, y, t)| \times \mathcal{K}^{-1})^2]^{-1}. \quad (8)$$

In addition to the critical parameter  $\mathcal{K}$  in the above equations, the number of iterations is also relevant for the noise reduction procedure. Following the best practices in the literature, the results have a  $\mathcal{K}$  scan range from 5 to 13 [71], while the number of iterations tested is 20 and 150 [72].

The idea behind bilateral filtering is to combine the nearby image values non-linearly. The pixels to be combined are chosen not only based on their geometric proximity, as is usual for filtering methods, but also based on their photometric similarity. The bilateral filter takes a weighted sum of the pixels in the neighbourhood based on both the spatial distance and the intensity distance. It has the significant advantage of smoothing an image while preserving structural information such as edges and fine details. This characteristic makes it particularly helpful in applications, such as medical images, where both noise reduction and preservation of structural information are crucial [68]. Bilateral filtering can, therefore, be seen as a blend of domain and range filtering:

$$I_b(x, y) = \frac{1}{C_b(x, y)} \sum_{s=-a}^a \sum_{t=-a}^a \exp\left(-\frac{s^2 + t^2}{2\sigma_d^2}\right) \times \exp\left(-\frac{|I(x-s, y-t) - I(x, y)|^2}{2\sigma_r^2}\right) I(x-s, y-t), \quad (9)$$

where  $\sigma_d$  and  $\sigma_r$  are filter parameters controlling the fall-off of the weights in spatial and intensity domains, respectively, providing flexibility to tailor the filtering process. The  $C_b$  is the normalisation constant that ensures that the intensity of the pixels in the resulting image remains consistent.

$$C_b(x, y) = \sum_{s=-a}^a \sum_{t=-a}^a \exp\left(-\frac{s^2 + t^2}{2\sigma_d^2}\right) \exp\left(-\frac{|I(x-s, y-t) - I(x, y)|^2}{2\sigma_r^2}\right). \quad (10)$$

The spatial standard deviation  $\sigma_d$  determines how many neighbouring pixels affect each other, resulting in increased smoothing over larger regions with higher values of  $\sigma_d$ . In this specific case,  $\sigma_d = 5$  has been predetermined on the basis of earlier work [73]. The parameter  $\sigma_r$  significantly impacts the filter performance, as it dictates the extent to which the neighbouring pixels interact and influence each other within the filtering operation. The values used here for testing are  $\sigma_r = 3, 5,$  and  $7$  (coloured values typical used), and a very large value of  $15$  is used to analyse the impact.

For a better quantification of the predicted segmentation, five metrics have been computed based on the values of true-positive (TP), false-positive (FP), true-negative (TN), and false-negative (FN), where TP represents the number of pixels correctly classified as a tumour, TN represents the number of pixels correctly classified as no tumour, FP represents the number of pixels incorrectly classified as tumour, and FN represents the number of pixels incorrectly classified as no tumour. The dice coefficient is a commonly used statistic for assessing segmentation accuracy by measuring the similarity between predicted and ground-truth segmentation. This metric is critical for evaluating the performance of image analysis algorithms, as it quantifies how closely the predicted segmentation matches the actual segmentation. The dice coefficient is given as follows [74]:

$$\text{Dice} = \frac{2\text{TP}}{2\text{TP} + \text{FP} + \text{FN}}. \quad (11)$$

The current algorithm employs a loss parameter to measure the training progress across epochs, which is defined as follows:

$$\text{Dice loss} = 1 - \text{Dice}. \quad (12)$$

To ensure the stability of the model, an early stop criterion is implemented, with the requirement that the loss value should remain unchanged and the learning rate set to a minimum of  $1 \times 10^{-7}$ . Additionally, a patience parameter of 20 epochs, combined with the loss function, is utilised to mitigate overfitting issues. These measures are essential for accurate segmentation and improved model performance over time.

When evaluating the effectiveness of different image segmentation algorithms or datasets, a single metric often fails to capture the whole picture. In this work, additional metrics have been taken into account. The Jaccard index is as follows [75]:

$$\text{Jaccard} = \frac{\text{TP}}{\text{TP} + \text{FP} + \text{FN}} \quad (13)$$

which, like the dice coefficient, allows us to assess the similarity between two sets. Although both coefficients range from 0 (no similarity) to 1 (complete similarity), the dice coefficient tends to give more weight to common elements, whereas the Jaccard index provides a more balanced measure concerning the entire set.

In tumour segmentation, accuracy is the proportion of correctly classified pixels (both tumour and non-tumour) out of the total pixels. Although it provides a general indication of model performance, accuracy can be misleading in medical imaging due to class imbalance, which occurs when the tumour region is significantly smaller than the background. A high accuracy could just represent the correct classification of non-tumour pixels, leaving out the model's ability to recognise the tumour itself. As a result, accuracy should be assessed alongside measurements such as precision, recall, and the F1 score for a more thorough evaluation.

$$\text{Accuracy} = \frac{\text{TP} + \text{TN}}{\text{TN} + \text{TP} + \text{FN} + \text{FP}}. \quad (14)$$

Recall, also known as sensitivity, assesses the segmentation algorithm's capacity to correctly detect all tumour pixels in the ground truth. It is determined as the ratio of true positive pixels (tumour pixels that have been correctly recognised) to the total tumour



pixels. A high recall suggests that the system noticed the majority of the tumour pixels, reducing false negatives:

$$\text{Recall} = \frac{\text{TP}}{\text{TP} + \text{FN}}. \quad (15)$$

Precision is defined as the ratio of true positive pixels (correctly identified tumour pixels) to the total number of pixels classified as tumours by the model (true positives plus false positives). High precision means that the algorithm has a low false-positive rate, implying that it rarely misidentifies non-tumour pixels as tumour:

$$\text{Precision} = \frac{\text{TP}}{\text{TP} + \text{FP}}. \quad (16)$$

It should be noted that recall and precision are very sensitive to the size of the segmented regions, penalising errors in small areas. To overcome this limitation, the F1 score is often used. The F1 index is the harmonic mean of precision and recall, resulting in a single statistic that accounts for both false positives and false negatives. This is especially relevant in the context of segmentation, where segment sizes might vary significantly, and class distributions can be unbalanced. It is based on the general expression with  $\beta = 1$  [76]:

$$F_{\beta} = \frac{(\beta^2 + 1) \times \text{Precision} \times \text{Recall}}{\beta^2 \times \text{Precision} + \text{Recall}}. \quad (17)$$

In the case of  $\beta = 1$ , it can be shown that  $F_1 = \text{Dice}$  for binary classification, except if different weights are assigned to precision and recall in the  $F_1$  score calculation.

### 3. Results and Discussion

Figure 1a shows a standard CE-MRI from the dataset used in this study. The subtle modifications of the filtering procedure are further illustrated by highlighting the distinctions between the filtered image and the original by plotting the absolute difference between the two images. The curved distortion observed at the boundaries of the figures is a consequence specific to the dataset that contains this particular artefact. Panel (b) shows the case of the median filter that displays certain nuances and edges of the original image, indicating a modest similarity to the initial image. In panel (c), after the Gaussian filter is applied, the image deviates from the original, and numerous characteristics are distinct from the original image. In panel (e), the impact of the anisotropic diffusion filter is shown, which deviates the most from the original. In summary, it is predictable that the results obtained for the image with the bilateral filter will be very similar to the ones obtained from the original. Finally, in panel (d), it becomes apparent that the image after the bilateral filter bears a strong resemblance to the original, with minimal remaining disparities between the two, mostly from noise reduction, thereby making it extremely challenging to discern any edges or subtleties from the initial image. However, the filter contributes to the enhancement of image quality by diminishing noise levels while effectively retaining the characteristics of the tumour.

This study focuses on the impact of image processing on segmentation using small datasets. The parameters of image filter processing collectively influence the ability to reduce noise while preserving important details, such as edges. Table 2 and Figure 2a display the Gaussian filter performance for varying kernel sizes while training the U-Net algorithm in the image validation set. The model consistently attains a high level of accuracy, reducing dice loss values across all scenarios. However, the increased kernel-size dataset requires an additional 10 epochs for the numerical solution to reach stability. This extension in time is a direct result of the larger kernel's tendency to soften pronounced characteristics within the training data, thereby posing obstacles in image segmentation tasks. Although there are slight discrepancies in the results produced by the three different kernel sizes, the superior accuracy and precision are prominent for  $K = 5$ , a pattern that is similarly mirrored in the Jaccard index evaluation.

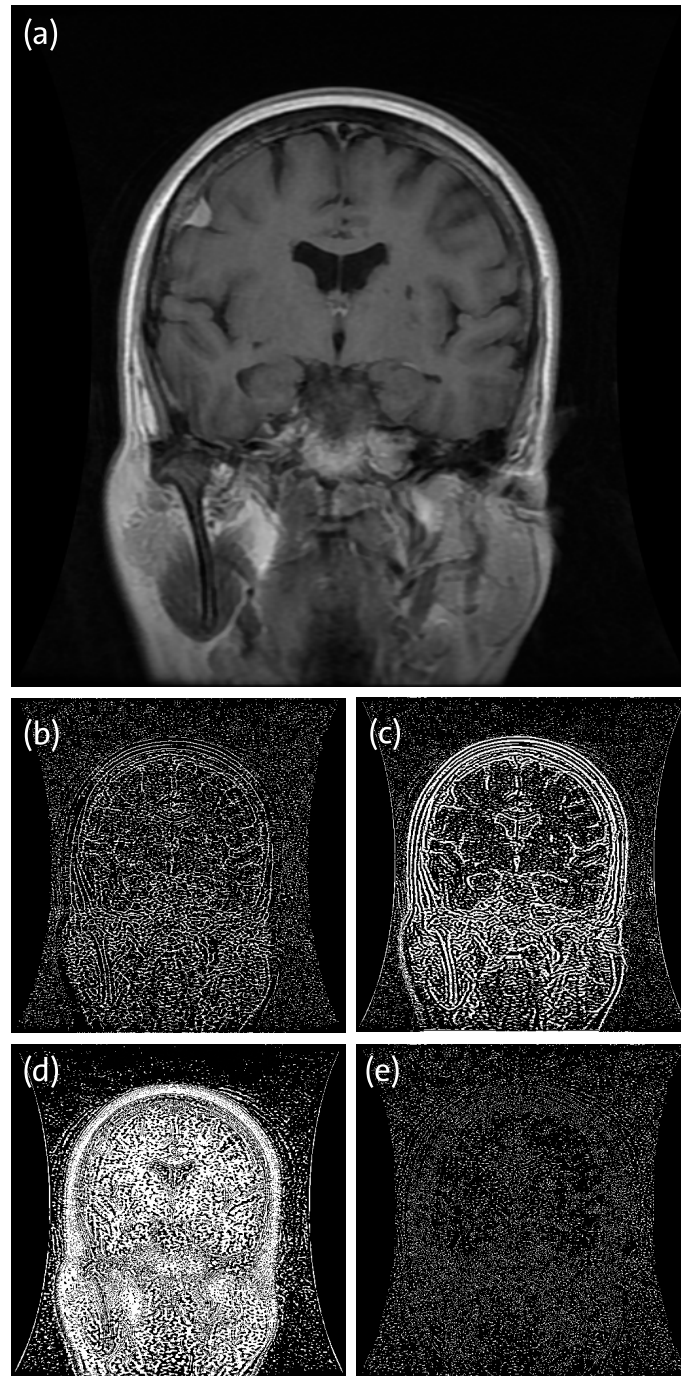


**Figure 1.** CE-MRI example from the dataset employed in this study (a). Panels (b–e) show the absolute difference values after applying the (b) median filter, (c) Gaussian filter, (d) bilateral filter, and (e) the anisotropic diffusion filter.

**Table 2.** Metrics for the image enhancing using several kernels sizes for the Gaussian filter.

Metric	$K = 3$	$K = 5$	$K = 7$
$F_1$	0.7518	0.7555	0.7535
Jaccard index	0.6677	0.6711	0.6688
Recall	0.7504	0.7330	0.7333
Precision	0.8061	0.8346	0.8340
Accuracy	0.9937	0.9941	0.9941

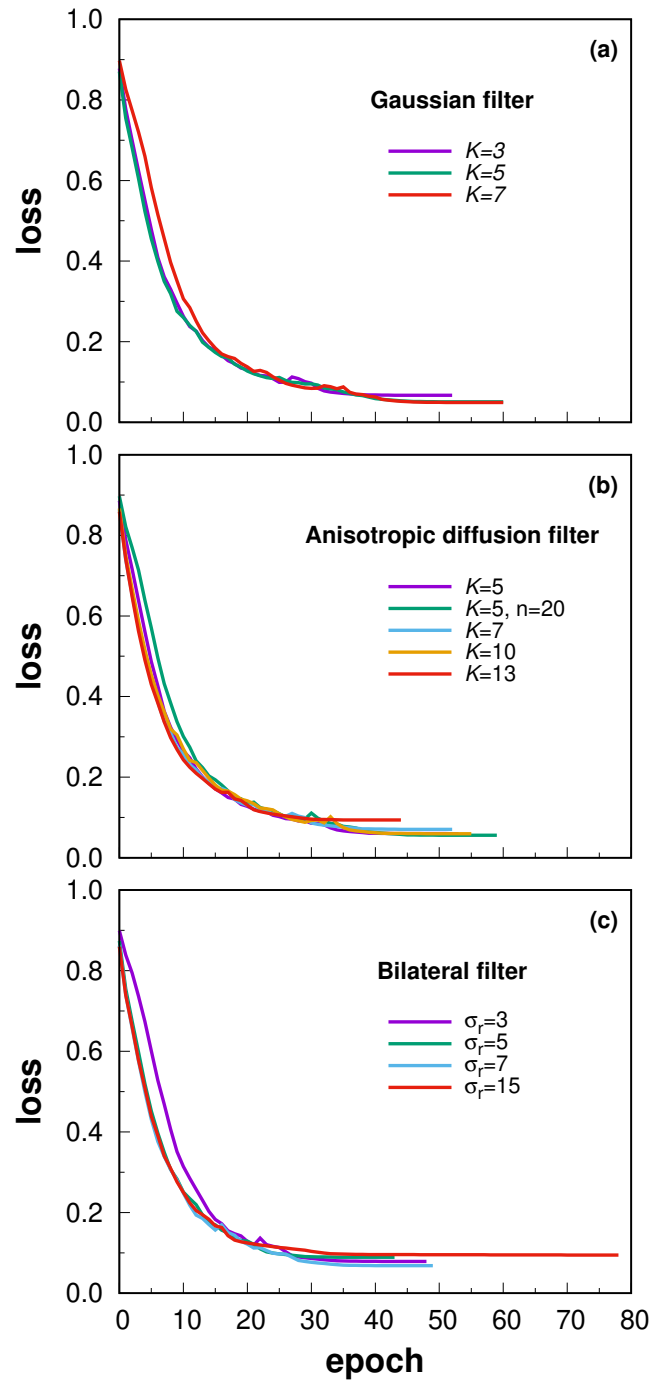


**Figure 2.** Training loss performance of the U-Net model considering the validation dataset for the different pre-processing images: (a) Gaussian, (b) anisotropic diffusion, and (c) bilateral filters. For the anisotropic diffusion filter, the value of interactions has been fixed at  $n = 150$ , except for  $K = 5$ ,  $n = 20$ , as indicated in the graph key.

For the anisotropic filter, three parameters have been analysed, and a summary of the best results is shown in Table 3 and Figure 2b. The functional form of the diffusion coefficient has been studied in Equations (7) and (8). It has been observed that the metrics are very similar between the use of the two functions. For example, the Jaccard index reported for  $K = 7$  and  $n = 150$  is 0.6318 when using Equation (8). However, when using the diffusion coefficient of Equation (7), a Jaccard index of 0.6339 is obtained. Due to such slightly improved results in segmentation, all remaining reported calculations employ Equation (7). Lower values of the  $K$  parameter yield better results, although the

accuracy remains similar. For example, precision improves by about 4% when  $\mathcal{K}$  decreases from 13 to 5, while the Jaccard index ranges from 0.6165 to 0.6545. It should be noted that smaller values of  $\mathcal{K}$  lead to a filtered image that is closer to the original without much noise reduction [67]. Previous works on denoising of images propose a value of  $\mathcal{K} = 6$  for 2D MRI, based on the contrast parameter for the edges of the structures [65,67], which closely follows the best value reported here for U-Net segmentation. Finally, the impact of the number of iterations  $n$ , where a large value implies a more denoised image, has been studied. For the best value of  $\mathcal{K}$ , the number of iterations of  $n = 20$  has been studied and also reported in Table 3. The general segmentation uses almost 10 epochs more than the corresponding one for  $n = 150$ , achieving more accurate results. The Jaccard index is improved by  $\sim 3\%$ , with a recall of 0.82032 and an accuracy of 0.99391.

**Table 3.** Summary of metrics for image enhancing using  $\mathcal{K}$  and  $n$  for the anisotropic diffusion filter. In all cases here reported, the diffusion coefficient is defined by Equation (7).

Metric	$\mathcal{K} = 5$ $n = 20$	$\mathcal{K} = 5$ $n = 150$	$\mathcal{K} = 7$ $n = 150$	$\mathcal{K} = 10$ $n = 150$	$\mathcal{K} = 13$ $n = 150$
$F_1$	0.7531	0.7377	0.7192	0.7101	0.7023
Jaccard index	0.6680	0.6545	0.6339	0.6258	0.6165
Recall	0.7400	0.7214	0.7082	0.6955	0.6855
Precision	0.8203	0.8167	0.7968	0.7911	0.7820
Accuracy	0.9939	0.9939	0.9932	0.9932	0.9931

In the scenario of using the bilateral filter, the pivotal parameter that significantly affects the performance of the filter is  $\sigma_r$ . Four different values were used to assess the influence of  $\sigma_r$  on the training and validation of the model, as described in Table 4. Panel (c) of Figure 2 illustrates the evolution of the loss parameter over the epochs. Two main distinctions are observable in the plot. Initially, for  $\sigma_r = 3$ , higher loss values are evident in the early epochs, running almost parallel to the other curves. This suggests that the smoothing effect might result in more intricate structures in the images as a result of the utilisation of small neighbourhood pixels. The graph also shows a significant increase in the number of epochs required for model training. The smoother process with the larger kernel complicates the analysis of the image features needed for segmentation. Minor differences in the metrics can be seen in Table 4, with precision and the Jaccard index showing the most notable variations. In all cases, the precision is 0.9940, and for  $\sigma_r = 5$ , there are high precision values of 0.8352 and a Jaccard index of 0.6849.

**Table 4.** Metrics for image enhancing using several values of  $\sigma_r$  for the bilateral filter.

Metric	$\sigma_r = 3$	$\sigma_r = 5$	$\sigma_r = 7$	$\sigma_r = 15$
$F_1$	0.7507	0.7696	0.7576	0.7401
Jaccard index	0.6637	0.6849	0.6722	0.6561
Recall	0.7437	0.7563	0.7440	0.7324
Precision	0.8168	0.8352	0.8279	0.8073
Accuracy	0.9940	0.9940	0.9939	0.9939

Figure 3 shows the progression of loss while training the U-Net algorithm on the image validation set. All loss curves have a rapid drop within the first 10–15 epochs. This shows that the U-Net model can quickly learn the fundamental properties of the data, regardless of the type of pre-processing used. The figure also illustrates that the model reaches stability approximately 10 epochs faster, compared to the original images when trained on the bilateral and median filter datasets. It is interesting to note that anisotropic diffusion and Gaussian filters require a similar amount of epochs to the original set. Additionally, it is notable that the significant image smoothing produced by the bilateral filter results in higher loss values in the initial 15 epochs, while the subsequent filtering processes show minimal change compared to the original dataset. Ultimately, all datasets converge to similar values of around  $\sim 0.05$ – $0.08$ , with the bilateral filter dataset being slightly higher.

In all cases, certain instabilities typically arise between 20–30 epochs. These instabilities are often linked to flat areas in multidimensional weight space, which can result in the emergence of local minima. To address this problem, the approach of “maintaining the best weights” during the training phase has been used, as detailed in [77]. This method not only serves as a reliable tool to mitigate potential training divergence but also helps prevent overfitting.

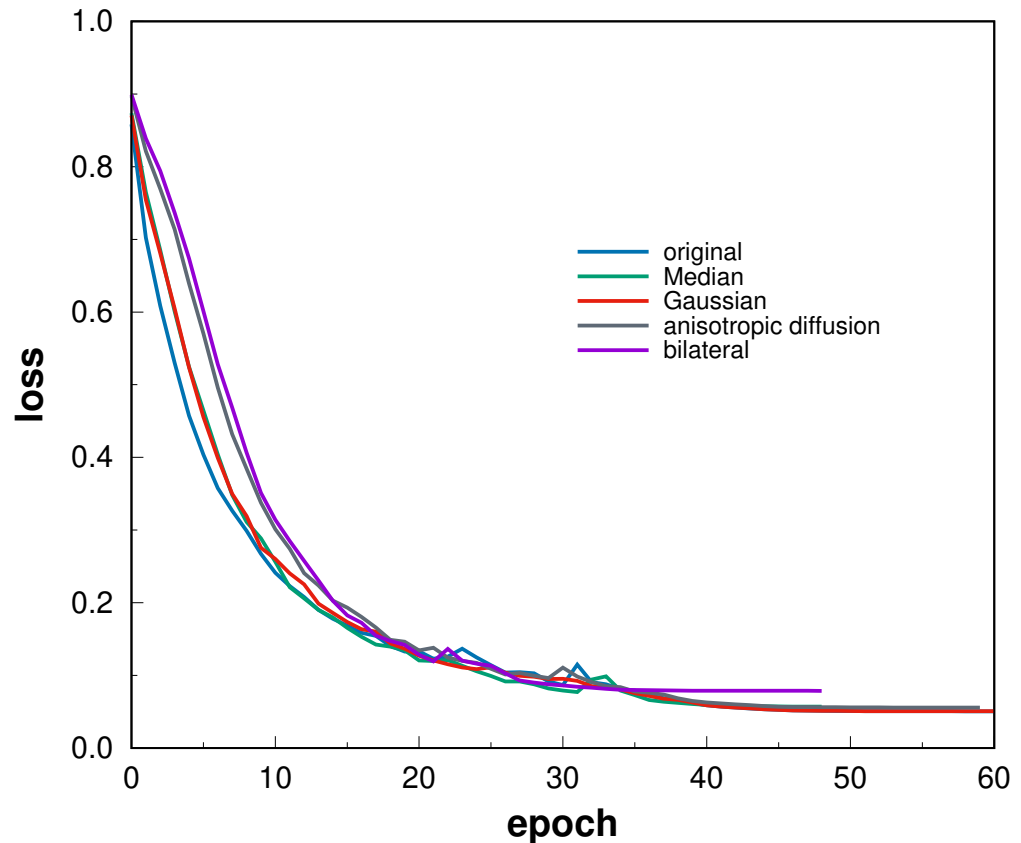


**Figure 3.** Training loss performance of the U-Net model considering the validation dataset and filtered images.

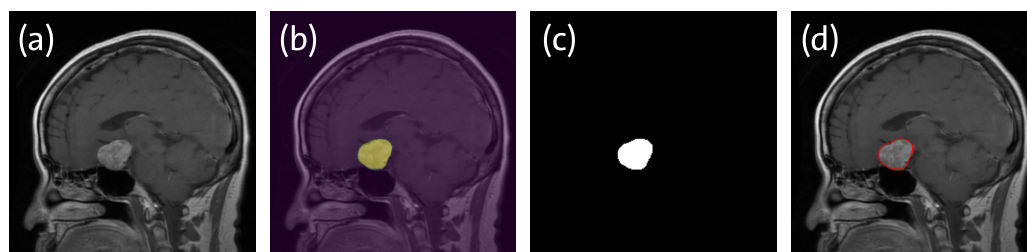
Since the multifaceted approach ensures a robust evaluation, it enables the identification of the most suitable algorithm for a specific image segmentation task. Table 5 collects the metrics for the entire set of test images. In every single test case that has been conducted, the accuracy level exceeds 0.995, demonstrating a notably high percentage of accurately classified mask pixels. As anticipated, the implementation of Gaussian and median filters results in decreased recall values because they work to diminish noise, which may also remove certain important image characteristics necessary for effective segmentation and classification purposes. The same happens with the anisotropic diffusion filter, in which the performance is not substantially changed by the application of the filter. This is probably due to the smoothing of the major structures of the original images and the small dataset used. Note that a high recall value ensures that the algorithm does not miss crucial details in the image.

The major differences between the results of the original and bilateral filter datasets can be found in the  $F_1$  score and the Jaccard index, the latter being useful to assess the precision and accuracy of segmentation masks. The use of a bilateral filter has been shown to improve the overall quality of the final results. A similar trend can be observed with the  $F_1$  score, which offers a more advanced approach to combining the benefits of precision and recall, which involve the proportion of pixels of the predicted object that correctly belongs to the object.

**Table 5.** Metrics of the four models proposed in this work considering the test set and the highest Jaccard index image.

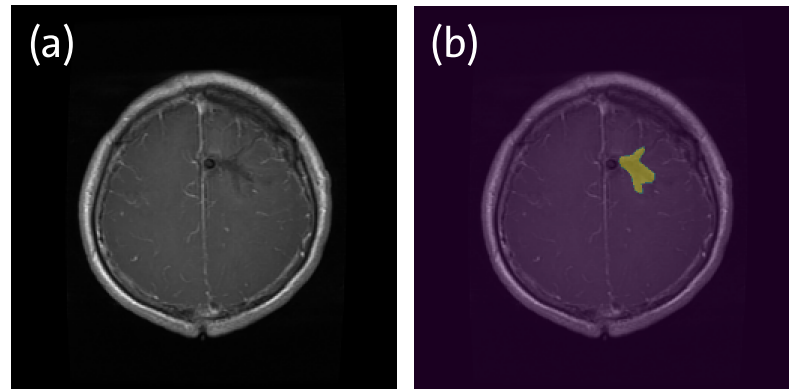
Metric	Original Image	Median Filter $\mathcal{N} = 3$	Gaussian Filter $K = 5$	Anisotropic Diffusion Filter $\mathcal{K} = 5, n = 20$	Bilateral Filter $\sigma_r = 5, \sigma_d = 5$
Test set					
$F_1$	0.7658	0.7495	0.7555	0.7531	0.7696
Jaccard index	0.6815	0.6664	0.6711	0.6680	0.6849
Recall	0.7557	0.7493	0.7330	0.7400	0.7563
Precision	0.8338	0.8110	0.8346	0.8203	0.8352
Accuracy	0.9941	0.9938	0.9941	0.9939	0.9940
Image with highest Jaccard index					
$F_1$	0.9793	0.9789	0.9820	0.9788	0.9859
Jaccard index	0.9594	0.9646	0.9587	0.9654	0.9721
Recall	0.9898	0.9728	0.9875	0.9873	0.9842
Precision	0.9689	0.9851	0.9764	0.9787	0.9842
Accuracy	0.999	0.9994	0.9995	0.9995	0.9996

Table 5 also presents a comprehensive set of metrics related to the image that has the highest value of the Jaccard index. In the illustrative Figure 4, a detailed portrayal of the segmentation process is depicted for this particular image. Panel (a) provides a glimpse of the image after bilateral filtering, while panels (b) and (c) offer views of the original mask and the predicted mask, respectively. This visual presentation serves to highlight the remarkable success achieved in the study, vividly displaying the model's exceptional performance in accomplishing the segmentation objective with an impressive accuracy of 0.9996. Subsequent to undergoing bilateral and partially in Gaussian filtering processes, all metrics exhibited notable enhancements compared to the original image. The application of the more conservative median filter smooths out the image features and diminishes the overall segmentation capabilities.

**Figure 4.** Example of the segmentation process for the image with the highest value of the Jaccard index: (a) image after bilateral filtering of the original image; (b) original mask; (c) obtained mask; (d) sobreposition of estimated mask contour in the image.

Some images can pose challenges in the detection of tumours due to specific characteristics. Analysing these images thoroughly to understand their unique characteristics is vital for improving the accuracy of tumour detection methods. Figure 5 depicts one of the most difficult segmentation images in this work. Panel (a) reveals the low contrast of the image, making it difficult to locate the tumour, which resembles sickle cell disease [78]. This similarity can be especially challenging in cases of significant brain abnormalities or acute vascular lesions in patients with stroke symptoms [79]. Two potential strategies may enhance our model. An approach is to increase the number of low-contrast images to improve learning with U-Net. Another strategy, in conjunction with pre-processing and adjusting the size of the dataset, involves improving the contrast of these images [80]. For example, Chandra et al. [81] used deep learning techniques for multi-contrast image reconstruction methods based on at least one pre-existing image.





**Figure 5.** Example of typical segmentation failure due to a low-contrast image: (a) original image and (b) original mask.

Thus far, a comparative analysis of segmentation performance due to the denoising of the original images has been carried out quantitatively using statistical metrics. As stated in the Introduction, a current trend over sustainability is emerging due to the need to reduce the emissions of GHG in radiology and to minimise resource consumption in the use of artificial intelligence. The use of filters and small datasets follow the best practices to reduce computational costs. In this particular case, typical values of 0.1 s/CUDA core per iteration and 8 s/epoch/CUDA core have been observed for the U-Net training. It has been shown that for a moderate size of image datasets, the results can be improved by filtering compared to the raw images. For example, denoising with the bilateral filter reduces 12 epochs compared to the original dataset, which reduces computational time in  $\sim 16$  h. It should be emphasised that denoising with the anisotropic diffusion filter requires additional computational time [82]. The filter's iterative nature necessitates multiple passes over the image to achieve effective smoothing while preserving edges. Each iteration involves complex calculations, making the process computationally intensive, especially for high-resolution images where the pixel count increases the computations. In real-time applications, where speed is crucial, the computational cost of anisotropic diffusion can be a limiting factor.

#### 4. Conclusions

This article presents a framework for automating brain tumour segmentation in CE-MRI scans. The study explores the effect of using different smoothing filters on images for tumour detection and segmentation within the U-Net framework. The proposed algorithm effectively captures both contextual information and precise tumour location in segmentation tasks. With a limited image dataset and pre-processing, the algorithm demonstrates high accuracy, proving valuable in medical imaging applications where annotated data are frequently limited.

For the pre-processing of original images, four common filters have been employed in imaging enhancement: median, Gaussian, anisotropic diffusion, and bilateral. A comprehensive examination of essential parameters has been carried out to improve the measure and indirectly evaluate computational expenses depending on the number of epochs employed.

Through the analysis of the metrics, it is possible to conclude that the bilateral filter provides better results. Due to the size of existing datasets, the pre-processing speed of training the bilateral filter is a valuable asset when compared to the original images and the remaining filters. The iterative nature of the anisotropic diffusion filter increases computational time and makes it less attractive for real-time applications and large datasets. In the case of the Gaussian filter, an optimised kernel of size  $5 \times 5$  yielded superior results, whereas the larger kernel,  $7 \times 7$ , increased computational costs by approximately 10 epochs without notable enhancement in metrics. In the bilateral filter scenario, four parameters were examined, with  $\sigma_r = 5$  producing the most relevant metrics for segmentation. In this

case, further studies can be envisaged by also optimising the spatial standard deviation  $\sigma_d$ , which was outside the scope of the present work.

Future work on the topic is envisaged both in method and algorithm development as well as in clinical testing. To expedite the process and minimise doctor intervention, the contour initialisation will be automated using a pre-trained neural network through transfer learning. This serves as a tumour detection phase, where the detector generates a bounding box around the tumour location prior to the geometric active contour step. This less detailed information is expected to enable faster training and reduce computing resource requirements. Initialising the contour of the level-set segmentation with the bounding box from the detection network requires extra caution. An expanding level set model can be employed to minimise the likelihood of front collapse. By improving image pre-processing capabilities, even the most intricate segmentation challenges associated with various conditions can be addressed and segmented effectively. Then, it can support medical professionals in diagnostic procedures, treatment planning, and research efforts. Overall, segmentation is computationally intensive, making it important to balance performance with available resources, especially in real-time applications.

**Author Contributions:** Conceptualization, S.R., V.V. and P.J.S.B.C.; Methodology, S.R., V.V. and P.J.S.B.C.; Investigation, S.R., V.V. and P.J.S.B.C.; Writing—review and editing, S.R., V.V. and P.J.S.B.C. All authors have read and agreed to the published version of the manuscript.

**Funding:** The Coimbra Chemistry Centre is supported by the FCT through the projects DOI: 10.54499/UIDB/00313/2020 and DOI: 10.54499/UIDP/00313/2020. P.J.S.B.C. acknowledges the project DOI: 10.54499/DL57/2016/CP1370/CT0050.

**Data Availability Statement:** The data presented in this study are openly available in <https://www.kaggle.com/datasets/nikhilroxtomar/brain-tumor-segmentation> (accessed on 10 February 2024) from the dataset originating from ref. [32] (<https://doi.org/10.1371/journal.pone.0140381>).

**Conflicts of Interest:** The authors declare no conflicts of interest.

## References

1. Tiwari, A.; Srivastava, S.; Pant, M. Brain tumor segmentation and classification from magnetic resonance images: Review of selected methods from 2014 to 2019. *Pattern Recognit. Lett.* **2020**, *131*, 244–260. [[CrossRef](#)]
2. American Brain Tumour Association. *About Brain Tumors: A Primer for Patients & Caregivers (for Patients & Caregivers)*; American Brain Tumour Association: Chicago, IL, USA, 2020.
3. Louis, D.N.; Perry, A.; Wesseling, P.; Brat, D.J.; Cree, I.A.; Figarella-Branger, D.; Hawkins, C.; Ng, H.K.; Pfister, S.M.; Reifenberger, G.; et al. The 2021 WHO classification of tumors of the central nervous system: A summary. *Neuro-Oncology* **2021**, *23*, 1231–1251. [[CrossRef](#)] [[PubMed](#)]
4. Joseph, R.P.; Singh, C.S.; Manikandan, M. Brain tumor MRI image segmentation and detection in image processing. *Int. J. Res. Eng. Technol.* **2014**, *3*, 1–5. [[CrossRef](#)]
5. Rodríguez-Camacho, A.; Flores-Vázquez, J.G.; Moscardini-Martelli, J.; Torres-Ríos, J.A.; Olmos-Guzmán, A.; Ortiz-Arce, C.S.; Cid-Sánchez, D.R.; Pérez, S.R.; Macías-González, M.D.S.; Hernández-Sánchez, L.C.; et al. Glioblastoma treatment: State-of-the-art and future perspectives. *Int. J. Mol. Sci.* **2022**, *23*, 7207. [[CrossRef](#)] [[PubMed](#)]
6. Hammoud, M.A.; Sawaya, R.; Shi, W.; Thall, P.F.; Leeds, N.E. Prognostic significance of preoperative MRI scans in glioblastoma multiforme. *J. Neuro-Oncol.* **1996**, *27*, 65–73. [[CrossRef](#)] [[PubMed](#)]
7. Semelka, R.C.; Armao, D.M.; Elias Junior, J.; Huda, W. Imaging strategies to reduce the risk of radiation in CT studies, including selective substitution with MRI. *J. Magn. Reson. Imaging* **2007**, *25*, 900–909. [[CrossRef](#)]
8. Abdusalomov, A.B.; Mukhiddinov, M.; Whangbo, T.K. Brain tumor detection based on deep learning approaches and magnetic resonance imaging. *Cancers* **2023**, *15*, 4172. [[CrossRef](#)]
9. Goyal, B.; Dogra, A.; Agrawal, S.; Sohi, B.S.; Sharma, A. Image denoising review: From classical to state-of-the-art approaches. *Inf. Fusion* **2020**, *55*, 220–244. [[CrossRef](#)]
10. Ahamed, M.F.; Hossain, M.M.; Nahiduzzaman, M.; Islam, M.R.; Islam, M.R.; Ahsan, M.; Haider, J. A review on brain tumor segmentation based on deep learning methods with federated learning techniques. *Comput. Med. Imaging Graph.* **2023**, *110*, 102313. [[CrossRef](#)]
11. Preim, B.; Botha, C. (Eds.) *Visual Computing for Medicine*; Morgan Kaufmann: Boston, MA, USA, 2014. [[CrossRef](#)]
12. Dora, L.; Agrawal, S.; Panda, R.; Abraham, A. State-of-the-art methods for brain tissue segmentation: A review. *IEEE Rev. Biomed. Eng.* **2017**, *10*, 235–249. [[CrossRef](#)]

13. Ragupathy, B.; Karunakaran, M. A deep learning model integrating convolution neuralnetwork and multiple kernel  $K$  means clustering for segmenting brain tumor in magnetic resonance images. *Int. J. Imaging Syst. Technol.* **2020**, *31*, 118–127. . [CrossRef]
14. Ramesh, S.; Sasikala, S.; Paramanandham, N. Segmentation and classification of brain tumors using modified median noise filter and deep learning approaches. *Multimed. Tools Appl.* **2021**, *80*, 11789–11813. [CrossRef]
15. Sathish, P.; Elango, N.M. Gaussian hybrid fuzzy clustering and radial basis neural network for automatic brain tumor classification in MRI images. *Evol. Intell.* **2022**, *15*, 1359–1377. [CrossRef]
16. Aljabri, M.; AlGhamdi, M. A review on the use of deep learning for medical images segmentation. *Neurocomputing* **2022**, *506*, 311–335. [CrossRef]
17. Liu, X.; Song, L.; Liu, S.; Zhang, Y. A review of deep-learning-based medical image segmentation methods. *Sustainability* **2021**, *13*, 1224. [CrossRef]
18. Wang, R.; Lei, T.; Cui, R.; Zhang, B.; Meng, H.; Nandi, A.K. Medical image segmentation using deep learning: A survey. *IET Image Process.* **2022**, *16*, 1243–1267. [CrossRef]
19. Kaur, R.; Doegar, A. Brain tumor segmentation using deep learning: Taxonomy, survey and challenges. In *Brain Tumor MRI Image Segmentation Using Deep Learning Techniques*; Chaki, J., Ed.; Academic Press: Cambridge, MA, USA, 2022; pp. 225–238. [CrossRef]
20. Gupta, A.; Dixit, M.; Mishra, V.K.; Singh, A.; Dayal, A. Brain tumor segmentation from MRI images using deep learning techniques. In Proceedings of the International Advanced Computing Conference, Hyderabad, India, 16–17 December 2022; Springer: Berlin/Heidelberg, Germany, 2022; pp. 434–448. .36. [CrossRef]
21. Liu, Z.; Tong, L.; Chen, L.; Jiang, Z.; Zhou, F.; Zhang, Q.; Zhang, X.; Jin, Y.; Zhou, H. Deep learning based brain tumor segmentation: A survey. *Complex Intell. Syst.* **2023**, *9*, 1001–1026. [CrossRef]
22. Keerthi, S.; Shettigar, Y.N.; Keerthana, K.; Divyashree, K.; Bhargavi, S. A review on brain tumor prediction using deep learning. In Proceedings of the 2023 International Conference on Advancement in Computation & Computer Technologies (InCACCT), Gharuan, India, 5–6 May 2023; IEEE: New York, NY, USA, 2023; pp. 155–160. [CrossRef]
23. Brain Tumor Segmentation (BraTS2020). Available online: <https://www.kaggle.com/datasets/awsaf49/brats2020-training-data> (accessed on 8 June 2024).
24. Mostafa, A.M.; Zakariah, M.; Aldakheel, E.A. Brain tumor segmentation using deep learning on MRI images. *Diagnostics* **2023**, *13*, 1562. [CrossRef]
25. Haritha, V.; Babu, J.J.; Saranya, R.; Yogaraja, C.; Rajalakshmi, S.; Manimegalai, L. Effective segmentation of brain tumors through the GOA algorithm using deep learning. In Proceedings of the 2023 2nd International Conference on Applied Artificial Intelligence and Computing (ICAIC), Salem, India, 4–6 May 2023; IEEE: New York, NY, USA, 2023; pp. 389–395. [CrossRef]
26. Al-Zoghby, A.M.; Al-Awadly, E.M.K.; Moawad, A.; Yehia, N.; Ebada, A.I. Dual Deep CNN for Tumor Brain Classification. *Diagnostics* **2023**, *13*, 2050. [CrossRef]
27. Shreeharsha, J. Brain tumor segmentation and classification using binomial thresholding-based bidirectional-long-short term memory. *Int. J. Intell. Syst.* **2024**, *17*, 149. [CrossRef]
28. Ali, M.; Gilani, S.O.; Waris, A.; Zafar, K.; Jamil, M. Brain tumour image segmentation using deep networks. *IEEE Access* **2020**, *8*, 153589–153598. [CrossRef]
29. Sadique, S.; Nishanthi, X.; Swaathy, V.; Mabisha, S.; Thanka, R.; Edwin, B. Brain tumor segmentation and evaluation empowered with deep learning. In Proceedings of the 2023 7th International Conference on Intelligent Computing and Control Systems (ICICCS), Madurai, India, 17–19 May 2023; IEEE: New York, NY, USA, 2023; pp. 305–312. [CrossRef]
30. Srinivas, B.; Sasibhushana Rao, G. Segmentation of multi-modal MRI brain tumor sub-regions using deep learning. *J. Electr. Eng. Technol.* **2020**, *15*, 1899–1909. [CrossRef]
31. Alhassan, A.; Zainon, W.M.N. BAT algorithm with fuzzy c-ordered means (BAFCOM) clustering segmentation and enhanced capsule networks (ECN) for brain cancer MRI images classification. *IEEE Access* **2020**, *8*, 201741–201751. [CrossRef]
32. Jamzad, M. A reliable ensemble-based classification framework for glioma brain tumor segmentation. *Signal Image Video Process.* **2020**, *14*, 1591–1599. [CrossRef]
33. Zhou, Z.; Rahman Siddiquee, M.M.; Tajbakhsh, N.; Liang, J. UNet++: A nested U-Net architecture for medical image segmentation. In *Deep Learning in Medical Image Analysis and Multimodal Learning for Clinical Decision Support*; Stoyanov, D., Taylor, Z., Carneiro, G., Syeda-Mahmood, T., Martel, A., Maier-Hein, L., Tavares, J.M.R., Bradley, A., Papa, J.P., Belagiannis, V., et al., Eds.; Springer: Cham, Switzerland, 2018; pp. 3–11. [CrossRef]
34. Micallef, N.; Seychell, D.; Bajada, C.J. Exploring the U-Net++ model for automatic brain tumor segmentation. *IEEE Access* **2021**, *9*, 125523–125539. [CrossRef]
35. Huang, H.; Lin, L.; Tong, R.; Hu, H.; Zhang, Q.; Iwamoto, Y.; Han, X.; Chen, Y.W.; Wu, J. UNet3+: A full-scale connected UNet for medical image segmentation. In Proceedings of the ICASSP 2020—2020 IEEE International Conference on Acoustics, Speech and Signal Processing (ICASSP), Barcelona, Spain, 4–8 May 2020; pp. 1055–1059. [CrossRef]
36. Qin, C.; Wu, Y.; Liao, W.; Zeng, J.; Liang, S.; Zhang, X. Improved U-Net3+ with stage residual for brain tumor segmentation. *BMC Med. Imaging* **2022**, *22*, 14. [CrossRef] [PubMed]
37. Henkelman, R.M. Measurement of signal intensities in the presence of noise in MR images. *Med. Phys.* **1985**, *12*, 232–233. [CrossRef]
38. Young, K.; Schuff, N. Measuring structural complexity in brain images. *NeuroImage* **2008**, *39*, 1721–1730. [CrossRef]

39. Pancholi, B.K.; Modi, P.S.; Chitaliya, N. A review of noise reduction filtering techniques for MRI images. In Proceedings of the 2022 5th International Conference on Contemporary Computing and Informatics (IC3I), Uttar Pradesh, India, 14–16 December 2022; pp. 954–960. [\[CrossRef\]](#)
40. Li, P.; Wang, H.; Yu, M.; Li, Y. Overview of image smoothing algorithms. *J. Phys.* **2021**, *1883*, 012024. [\[CrossRef\]](#)
41. Ishfaq, N. A review on comparative study of image-denoising in medical imaging. In *Deep Learning for Multimedia Processing Applications*; CRC Press: Boca Raton, FL, USA, 2024.
42. Kumar, R.R.; Priyadarshi, R. Denoising and segmentation in medical image analysis: A comprehensive review on machine learning and deep learning approaches. *Multimed. Tools Appl.* **2024**. [\[CrossRef\]](#)
43. Liu, Z.; Ma, C.; She, W.; Xie, M. Biomedical image segmentation using denoising diffusion probabilistic models: A comprehensive review and analysis. *Appl. Sci.* **2024**, *14*, 632. [\[CrossRef\]](#)
44. Doo, F.X.; Vosshenrich, J.; Cook, T.S.; Moy, L.; Almeida, E.P.; Woolen, S.A.; Gichoya, J.W.; Heye, T.; Hanneman, K. Environmental sustainability and AI in radiology: A double-edged sword. *Radiology* **2024**, *310*, e232030. [\[CrossRef\]](#) [\[PubMed\]](#)
45. Bovik, A.C. *Handbook of Image and Video Processing*; Elsevier: Amsterdam, The Netherlands, 2005.
46. Bourne, R. *Fundamentals of Digital Imaging in Medicine*; Springer: London, UK, 2010.
47. Ertürk, M.A.; Bottomley, P.A.; El-Sharkawy, A.M.M. Denoising MRI using spectral subtraction. *IEEE Trans. Biomed. Eng.* **2013**, *60*, 1556–1562. [\[CrossRef\]](#) [\[PubMed\]](#)
48. Patel, K.; Mewada, H.N. A review on different image de-noising methods. *Int. J. Recent Innov. Trends Comput. Commun.* **2014**, *2*, 155–159. [\[CrossRef\]](#)
49. Cheng, J.; Huang, W.; Cao, S.; Yang, R.; Yang, W.; Yun, Z.; Wang, Z.; Feng, Q. Enhanced performance of brain tumor classification via tumor region augmentation and partition. *PLoS ONE* **2015**, *10*, e0140381. [\[CrossRef\]](#)
50. Ronneberger, O.; Fischer, P.; Brox, T. U-Net: Convolutional networks for biomedical image segmentation. In Proceedings of the Medical Image Computing and Computer-Assisted Intervention—MICCAI 2015, Munich, Germany, 5–9 October 2015; Navab, N., Hornegger, J., Wells, W.M., Frangi, A.F., Eds.; Springer: Cham, Switzerland, 2015; pp. 234–241. [\[CrossRef\]](#)
51. Abadi, M.; Agarwal, A.; Barham, P.; Brevdo, E.; Chen, Z.; Citro, C.; Corrado, G.S.; Davis, A.; Dean, J.; Devin, M.; et al. TensorFlow: Large-scale machine learning on heterogeneous systems. In Proceedings of the 12th USENIX Conference on Operating Systems Design and Implementation, Savannah, GA, USA, 2–4 November 2016.
52. Ye, J.C.; Sung, W.K. Understanding Geometry of Encoder-Decoder CNNs. In Proceedings of the 36th International Conference on Machine Learning, PMLR, Long Beach, CA, USA, 9–15 June 2019; pp. 7064–7073.
53. Zhang, J.; Zeng, J.; Qin, P.; Zhao, L. Brain tumor segmentation of multi-modality MR images via triple intersecting U-Nets. *Neurocomputing* **2021**, *421*, 195–209. [\[CrossRef\]](#)
54. Zhou, S.; Nie, D.; Adeli, E.; Yin, J.; Lian, J.; Shen, D. High-resolution encoder–decoder networks for low-contrast medical image segmentation. *IEEE Trans. Image Process.* **2020**, *29*, 461–475. [\[CrossRef\]](#)
55. Allah, A.M.G.; Sarhan, A.M.; Elshennawy, N.M. Edge U-Net: Brain tumor segmentation using MRI based on deep U-Net model with boundary information. *Expert Syst. Appl.* **2023**, *213*, 118833. [\[CrossRef\]](#)
56. Li, Z.; Liu, F.; Yang, W.; Peng, S.; Zhou, J. A Survey of Convolutional Neural Networks: Analysis, Applications, and Prospects. *IEEE Trans. Neural Netw. Learn. Syst.* **2022**, *33*, 6999–7019. [\[CrossRef\]](#)
57. Michelucci, U. *Applied Deep Learning: A Case-Based Approach to Understanding Deep Neural Networks*; Apress: New York, NY, USA, 2018. [\[CrossRef\]](#)
58. Ghosh, S.; Das, N.; Das, I.; Maulik, U. Understanding deep learning techniques for image segmentation. *ACM Comput. Surv.* **2019**, *52*, 1–35. [\[CrossRef\]](#)
59. Huang, L.; Qin, J.; Zhou, Y.; Zhu, F.; Liu, L.; Shao, L. Normalization techniques in training DNNs: Methodology, analysis and application. *IEEE Trans. Pattern Anal. Mach. Intell.* **2023**, *45*, 10173–10196. [\[CrossRef\]](#) [\[PubMed\]](#)
60. Apicella, A.; Donnarumma, F.; Isgrò, F.; Prevete, R. A survey on modern trainable activation functions. *Int. J. Neural Netw.* **2021**, *138*, 14–32. [\[CrossRef\]](#) [\[PubMed\]](#)
61. Dubey, S.R.; Singh, S.K.; Chaudhuri, B.B. Activation functions in deep learning: A comprehensive survey and benchmark. *Neurocomputing* **2022**, *503*, 92–108. [\[CrossRef\]](#)
62. Akhtar, N.; Ragavendran, U. Interpretation of intelligence in CNN-pooling processes: A methodological survey. *Neural Comput. Appl.* **2020**, *32*, 879–898. [\[CrossRef\]](#)
63. Kumar, N.; Nachamai, M. Noise removal and filtering techniques used in medical images. *Orient. J. Comput. Sci. Technol.* **2017**, *10*, 103–113. [\[CrossRef\]](#)
64. Ali, H.M. A new method to remove salt & pepper noise in magnetic resonance images. In Proceedings of the 2016 11th International Conference on Computer Engineering & Systems (ICCES), Cairo, Egypt, 20–21 December 2016; pp. 155–160. [\[CrossRef\]](#)
65. Krissian, K.; Aja-Fernandez, S. Noise-driven anisotropic diffusion filtering of MRI. *IEEE Trans. Image Process.* **2009**, *18*, 2265–2274. [\[CrossRef\]](#)
66. Mishro, P.K.; Agrawal, S.; Panda, R.; Abraham, A. A Survey on State-of-the-Art Denoising Techniques for Brain Magnetic Resonance Images. *IEEE Rev. Biomed. Eng.* **2022**, *15*, 184–199. [\[CrossRef\]](#)
67. Gerig, G.; Kubler, O.; Kikinis, R.; Jolesz, F. Nonlinear anisotropic filtering of MRI data. *IEEE Trans. Med. Imaging* **1992**, *11*, 221–232. [\[CrossRef\]](#)



68. Zhang, M.; Gunturk, B.K. Multiresolution bilateral filtering for image denoising. *IEEE Trans. Image Process.* **2008**, *17*, 2324–2333. [[CrossRef](#)]
69. Chethan, K.S.; Swamy, R.K.; Sinchana, G.S.; Sowkya, H.K.; Sujith, J.; Choodarathnakara, A.L. Impact of bandwidth on LANDSAT-7 ETM+ image quality using gaussian filter: Bangalore, Karnataka State, India. In Proceedings of the 2019 1st International Conference on Advances in Information Technology (ICAIT), Chikmagalur, India, 25–27 July 2019; pp. 1–7. [[CrossRef](#)]
70. Gudbjartsson, H.; Patz, S. The rician distribution of noisy mri data. *Magn. Reson. Med.* **1995**, *34*, 910–914. [[CrossRef](#)]
71. Bajla, I.; Marušiak, M.; Šrámek, M. Anisotropic filtering of MRI data based upon image gradient histogram. In Proceedings of the Computer Analysis of Images and Patterns, Virtual Event, 28–30 September 2021; Chetverikov, D., Kropatsch, W.G., Eds.; Springer: Berlin/Heidelberg, Germany, 1993; pp. 90–97. [[CrossRef](#)]
72. Tsiotsios, C.; Petrou, M. On the choice of the parameters for anisotropic diffusion in image processing. *Pattern Recognit.* **2013**, *46*, 1369–1381. [[CrossRef](#)]
73. Tomasi, C.; Manduchi, R. Bilateral filtering for gray and color images. *IEEE Trans. Image Process.* **1998**, 839–846. [[CrossRef](#)]
74. Dice, L.R. Measures of the amount of ecologic association between species. *Ecology* **1945**, *26*, 297–302. [[CrossRef](#)]
75. Jaccard, P. The Distribution of the Flora in the Alpine Zone.1. *New Phytol.* **1912**, *11*, 37–50. [[CrossRef](#)]
76. Chinchor, N. MUC-4 evaluation metrics. In Proceedings of the 4th Conference on Message Understanding, MUC4'92, McLean, VA, USA, 16–18 June 1992; pp. 22–29. [[CrossRef](#)]
77. Géron, A. *Hands-on Machine Learning with Scikit-Learn, Keras, and TensorFlow*; O'Reilly: Springfield, MI, USA, 2019.
78. Stotesbury, H.; Kawadler, J.M.; Saunders, D.E.; Kirkham, F.J. MRI detection of brain abnormality in sickle cell disease. *Expert Rev. Hematol.* **2021**, *14*, 473–491. [[CrossRef](#)]
79. Neumann-Haefelin, T.; Moseley, M.E.; Albers, G.W. New magnetic resonance imaging methods for cerebrovascular disease: Emerging clinical applications. *Ann. Neurol.* **2000**, *47*, 559–570. [[CrossRef](#)]
80. Dewey, B.E.; Zhao, C.; Reinhold, J.C.; Carass, A.; Fitzgerald, K.C.; Sotirchos, E.S.; Saidha, S.; Oh, J.; Pham, D.L.; Calabresi, P.A.; et al. DeepHarmony: A deep learning approach to contrast harmonization across scanner changes. *Magn. Reson. Imaging* **2019**, *64*, 160–170. [[CrossRef](#)]
81. Chandra, S.S.; Bran Lorenzana, M.; Liu, X.; Liu, S.; Bollmann, S.; Crozier, S. Deep learning in magnetic resonance image reconstruction. *J. Med. Imaging Radiat. Oncol.* **2021**, *65*, 564–577. [[CrossRef](#)]
82. Gilboa, G.; Osher, S. Nonlocal operators with applications to image processing. *Multiscale Model. Simul.* **2009**, *7*, 1005–1028. [[CrossRef](#)]

**Disclaimer/Publisher's Note:** The statements, opinions and data contained in all publications are solely those of the individual author(s) and contributor(s) and not of MDPI and/or the editor(s). MDPI and/or the editor(s) disclaim responsibility for any injury to people or property resulting from any ideas, methods, instructions or products referred to in the content.